Author(s): Hinkkanen, Marko & Harnefors, Lennart & Luomi, Jorma

Title: Reduced-Order Flux Observers With Stator-Resistance Adaptation for Speed-Sensorless Induction Motor Drives

Year: 2010

Version: Post print

Please cite the original version:

Hinkkanen, Marko & Harnefors, Lennart & Luomi, Jorma. 2010. Reduced-Order Flux Observers With Stator-Resistance Adaptation for Speed-Sensorless Induction Motor Drives. IEEE Transactions on Power Electronics. Volume 25, Issue 5. 1173-1183. ISSN 0885-8993 (printed). DOI: 10.1109/tpel.2009.2039650.

Reduced-Order Flux Observers with Stator-Resistance Adaptation for Speed-Sensorless Induction Motor Drives

Marko Hinkkanen, *Member, IEEE,* Lennart Harnefors *Senior Member, IEEE*, and Jorma Luomi, *Member, IEEE*

***Abstract*—This paper deals with reduced-order flux observers with stator-resistance adaptation for speed-sensorless induction motor drives. A general analytical solution for the stabilizing observer gain is given. The gain has two free positive parameters (which depend on the operating point), whose selection significantly affects the damping, convergence rate, robustness, and other properties of the observer. The general stability conditions for the stator-resistance adaptation are derived. An observer design is proposed that yields a robust and well-damped system and requires a minimal amount of tuning work. The proposed observer design is experimentally tested using a 45-kW induction motor drive; stable operation at very low speeds under different loading conditions is demonstrated.**

***Index Terms*—Flux observer, stability conditions, speed sensorless, stator resistance estimation.**

I. Introduction

It is well known that speed-sensorless induction motor (IM) drives may have an unstable operating region at low speeds, typically in the regenerating mode [1]–[8]. Recently, general stability conditions for a full-order flux observer [6] and for a reduced-order observer [7] have been derived. Under these conditions, the local stability of the flux estimation is guaranteed at every operating point except the zero stator frequency, if the motor parameters are known.

In practice, variations of the stator resistance due to the temperature may cause stability problems at low speeds [9]. Different stator-resistance adaptation methods have been proposed to tackle this problem [8], [10]–[13]. Unfortunately, the dynamics of the stator-resistance adaptation are generally coupled with the flux and speed estimation dynamics. These couplings may cause unstable regions [13]. An in-depth stability analysis is usually omitted, since the resulting closed-loop systems become very complicated. In [11], however, a numerical stability analysis is presented when using a speed-adaptive observer based on the back electromotive force (EMF), whereas in [13], analytical stability conditions are derived in connection with a full-order flux observer.

The observer gain design is not trivial even if the analytical stability conditions are known. There are several free parameters that significantly affect the robustness, damping, convergence rate, and other properties of the system. For example, the stability conditions given in [6] for the full-order observer include three design parameters, which may depend on the operating point.

The preliminary version of this paper was presented at the IEEE Energy Conversion Congress and Exposition (ECCE), San Jose, CA, Sept. 20-24, 2009.

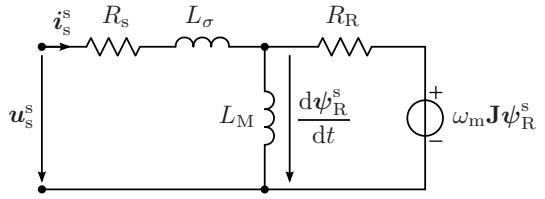

Fig. 1. Inverse-Γ model in stator coordinates (where $\omega_\mathrm{k} = 0$). The back EMF induced by the rotor flux is $\boldsymbol{e}^\mathrm{s} = \mathrm{d}\boldsymbol{\psi}_\mathrm{R}^\mathrm{s}/\mathrm{d}t$.

The main contributions of this paper are:

1) The stability conditions for a sensorless reduced-order observer, derived in [7], are formulated as a general stabilizing gain, which simplifies the tuning procedure.
2) A stator-resistance adaptation law is proposed, and analytical stability conditions are derived for the observer augmented with stator-resistance adaptation.
3) Based on these stability conditions, an easy-to-tune observer design is proposed.

The proposed design is comparatively simple, and it results in a robust and well-damped closed-loop system. The performance of the proposed observer design is evaluated using laboratory experiments with a 45-kW IM drive.

II. IM Model

In the next section, an observer which cannot be described in complex variables will be designed. Therefore, real space vectors will be used throughout the paper. For example, the definitions of the stator-current vector and its magnitude are

$$\boldsymbol{i}_\mathrm{s} = \begin{bmatrix} i_\mathrm{sx} \\ i_\mathrm{sy} \end{bmatrix}, \quad \|\boldsymbol{i}_\mathrm{s}\| = \sqrt{i_\mathrm{sx}^2 + i_\mathrm{sy}^2} \tag{1}$$

respectively, where the components i_sx and i_sy of the vector equal the real and imaginary parts of the complex space vector, respectively. The components and magnitudes of other vectors are denoted similarly. Vectors will be denoted by boldface lowercase letters and matrices by boldface uppercase letters. The matrix transpose will be marked with the superscript T. The identity matrix, the orthogonal rotation matrix, and the zero matrix are defined as

$$\mathbf{I} = \begin{bmatrix} 1 & 0 \\ 0 & 1 \end{bmatrix}, \quad \mathbf{J} = \begin{bmatrix} 0 & -1 \\ 1 & 0 \end{bmatrix}, \quad \mathbf{O} = \begin{bmatrix} 0 & 0 \\ 0 & 0 \end{bmatrix} \tag{2}$$

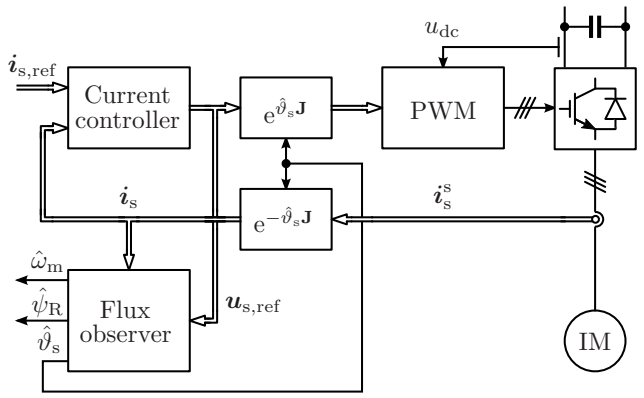

Fig. 2. Speed-sensorless rotor-flux-oriented controller when the flux observer is implemented in the estimated rotor-flux coordinates. The magnitude of the rotor-flux estimate is denoted by $\hat{\psi}_{\mathrm{R}} = \|\hat{\boldsymbol{\psi}}_{\mathrm{R}}\|$. The components of the current reference $\boldsymbol{i}_{\mathrm{s,ref}}$ are used for controlling the flux and the torque. The stator currents and the DC-link voltage u_{dc} are measured, and the reference voltage $\boldsymbol{u}_{\mathrm{s,ref}}$ obtained from the current controller is used for the flux observer.

respectively. Since $\mathbf{J}$ corresponds to the imaginary unit j, the notation is very similar to that obtained for complex space vectors.

The inverse-Γ model of an IM, shown in Fig. 1, is considered [14]. With the stator-current and rotor-flux vectors chosen as state variables, the electrical dynamics of the IM in general coordinates rotating at arbitrary angular speed ω_{k} are given by [15]

$$L_\sigma \frac{\mathrm{d}\boldsymbol{i}_{\mathrm{s}}}{\mathrm{d}t} + \omega_{\mathrm{k}} L_\sigma \mathbf{J}\boldsymbol{i}_{\mathrm{s}} = \boldsymbol{u}_{\mathrm{s}} - R_{\mathrm{s}}\boldsymbol{i}_{\mathrm{s}} - \boldsymbol{e} \tag{3}$$

$$\frac{\mathrm{d}\boldsymbol{\psi}_{\mathrm{R}}}{\mathrm{d}t} + \omega_{\mathrm{k}}\mathbf{J}\boldsymbol{\psi}_{\mathrm{R}} = \boldsymbol{e} \tag{4}$$

where L_σ is the leakage inductance, R_{s} the stator resistance, $\boldsymbol{u}_{\mathrm{s}} = [u_{\mathrm{sx}}, u_{\mathrm{sy}}]^{\mathrm{T}}$ the stator-voltage vector, and $\boldsymbol{\psi}_{\mathrm{R}} = [\psi_{\mathrm{Rx}}, \psi_{\mathrm{Ry}}]^{\mathrm{T}}$ is the rotor-flux vector. The back EMF induced by the rotor flux is

$$\boldsymbol{e} = R_{\mathrm{R}}\boldsymbol{i}_{\mathrm{s}} - (\alpha\mathbf{I} - \omega_{\mathrm{m}}\mathbf{J})\,\boldsymbol{\psi}_{\mathrm{R}} \tag{5}$$

where ω_{m} is the electrical rotor speed, R_{R} is the rotor resistance, and $\alpha = R_{\mathrm{R}}/L_{\mathrm{M}}$ is the inverse rotor time constant. From (3) it follows that the back EMF can also be expressed as

$$\boldsymbol{e} = \boldsymbol{u}_{\mathrm{s}} - R_{\mathrm{s}}\boldsymbol{i}_{\mathrm{s}} - L_\sigma \frac{\mathrm{d}\boldsymbol{i}_{\mathrm{s}}}{\mathrm{d}t} - \omega_{\mathrm{k}} L_\sigma \mathbf{J}\boldsymbol{i}_{\mathrm{s}}. \tag{6}$$

III. Reduced-Order Flux Observers

The estimate of the rotor-flux vector will be denoted by $\hat{\boldsymbol{\psi}}_{\mathrm{R}}$ and its angle with respect to the stator coordinates by $\hat{\vartheta}_{\mathrm{s}}$. A typical rotor-flux-oriented control system is depicted in Fig. 2, where the flux observer is implemented in estimated rotor-flux coordinates. In the following, the flux observer will be described in general coordinates rotating at arbitrary angular speed ω_{k}.

To avoid forbiddingly complicated equations, which would prevent analytical results from being derived, accurate parameter estimates are assumed, with the exception of the stator-resistance estimate $\hat{R}_{\mathrm{s}}$. Hence, an estimate for the back EMF can be calculated from (6) using the stator voltage[1] and the current as

$$\boldsymbol{e}' = \boldsymbol{u}_{\mathrm{s}} - \hat{R}_{\mathrm{s}}\boldsymbol{i}_{\mathrm{s}} - L_\sigma \frac{\mathrm{d}\boldsymbol{i}_{\mathrm{s}}}{\mathrm{d}t} - \omega_{\mathrm{k}} L_\sigma \mathbf{J}\boldsymbol{i}_{\mathrm{s}}. \tag{7}$$

Alternatively, the back EMF can be estimated based on (5)

$$\hat{\boldsymbol{e}} = R_{\mathrm{R}}\boldsymbol{i}_{\mathrm{s}} - (\alpha\mathbf{I} - \hat{\omega}_{\mathrm{m}}\mathbf{J})\,\hat{\boldsymbol{\psi}}_{\mathrm{R}} \tag{8}$$

where it is necessary to use the rotor-flux estimate $\hat{\boldsymbol{\psi}}_{\mathrm{R}}$ and the rotor-speed estimate $\hat{\omega}_{\mathrm{m}}$, since the actual values are not measured.

A. Reduced-Order Observer Structure

Starting from (4), a reduced-order observer combining the back-EMF estimates in (7) and (8) can be constructed as

$$\frac{\mathrm{d}\hat{\boldsymbol{\psi}}_{\mathrm{R}}}{\mathrm{d}t} + \omega_{\mathrm{k}}\mathbf{J}\hat{\boldsymbol{\psi}}_{\mathrm{R}} = \boldsymbol{e}' + \boldsymbol{K}(\hat{\boldsymbol{e}} - \boldsymbol{e}') \tag{9}$$

where $\boldsymbol{K}$ is a 2×2 observer gain matrix. Similar structures can be found in, e.g., [16], [15]. The structure (9) is selected, since it leads to simpler formulations of the observer gain in the case of speed-sensorless drives.

Selecting $\boldsymbol{K} = \mathbf{I}$, the well-known current model

$$\frac{\mathrm{d}\hat{\boldsymbol{\psi}}_{\mathrm{R}}}{\mathrm{d}t} + \omega_{\mathrm{k}}\mathbf{J}\hat{\boldsymbol{\psi}}_{\mathrm{R}} = R_{\mathrm{R}}\boldsymbol{i}_{\mathrm{s}} - (\alpha\mathbf{I} - \hat{\omega}_{\mathrm{m}}\mathbf{J})\,\hat{\boldsymbol{\psi}}_{\mathrm{R}} \tag{10}$$

is obtained. The current model cannot be directly used in speed-sensorless drives, since it depends on the rotor-speed estimate $\hat{\omega}_{\mathrm{m}}$. The pure voltage model

$$\frac{\mathrm{d}\hat{\boldsymbol{\psi}}_{\mathrm{R}}}{\mathrm{d}t} + \omega_{\mathrm{k}}\mathbf{J}\hat{\boldsymbol{\psi}}_{\mathrm{R}} = \boldsymbol{u}_{\mathrm{s}} - \hat{R}_{\mathrm{s}}\boldsymbol{i}_{\mathrm{s}} - L_\sigma \frac{\mathrm{d}\boldsymbol{i}_{\mathrm{s}}}{\mathrm{d}t} - \omega_{\mathrm{k}} L_\sigma \mathbf{J}\boldsymbol{i}_{\mathrm{s}} \tag{11}$$

is obtained by selecting $\boldsymbol{K} = \mathbf{O}$. The voltage model does not depend on the rotor-speed estimate, but it cannot be used in practice due to its well-known stability problems.

The rotor-speed estimate can be computed using the slip relation

$$\hat{\omega}_{\mathrm{m}} = \hat{\omega}_{\mathrm{s}} - \frac{R_{\mathrm{R}}\boldsymbol{i}_{\mathrm{s}}^{\mathrm{T}}\mathbf{J}\hat{\boldsymbol{\psi}}_{\mathrm{R}}}{\|\hat{\boldsymbol{\psi}}_{\mathrm{R}}\|^2}. \tag{12}$$

That is, the component of the back-EMF estimate in (8) perpendicular to the rotor-flux estimate is used for speed estimation. The angular speed $\hat{\omega}_{\mathrm{s}} = \mathrm{d}\hat{\vartheta}_{\mathrm{s}}/\mathrm{d}t$ of the rotor flux estimate can be generally expressed as

$$\hat{\omega}_{\mathrm{s}} = \omega_{\mathrm{k}} + \frac{\left(\frac{\mathrm{d}\hat{\boldsymbol{\psi}}_{\mathrm{R}}}{\mathrm{d}t}\right)^{\mathrm{T}}\mathbf{J}\hat{\boldsymbol{\psi}}_{\mathrm{R}}}{\|\hat{\boldsymbol{\psi}}_{\mathrm{R}}\|^2}. \tag{13}$$

The last term vanishes if the observer is implemented in estimated rotor-flux coordinates, i.e. $\hat{\omega}_{\mathrm{s}} = \omega_{\mathrm{k}}$.

[1] In the implementation, the stator voltage is not measured but the reference voltage $\boldsymbol{u}_{\mathrm{s,ref}}$ obtained from the current controller is used for the flux observer according to Fig. 2.

B. General Stabilizing Observer Gain

It is preferable that the flux observer (9) does not include the rotor-speed estimate $\hat{\omega}_\mathrm{m}$, i.e. the observer should be *inherently sensorless* [16]. The back-EMF estimate $\hat{\boldsymbol{e}}$ in (8) depends on $\hat{\omega}_\mathrm{m}$, but its component in the direction of $\hat{\boldsymbol{\psi}}_\mathrm{R}$ is independent of the rotor speed estimate. That is, in the scalar product

$$\hat{\boldsymbol{\psi}}_\mathrm{R}^\mathrm{T}\hat{\boldsymbol{e}} = \hat{\boldsymbol{\psi}}_\mathrm{R}^\mathrm{T}\left(R_\mathrm{R}\boldsymbol{i}_\mathrm{s} - \alpha\hat{\boldsymbol{\psi}}_\mathrm{R}\right) \tag{14}$$

the term proportional to $\hat{\omega}_\mathrm{m}$ vanishes, since $\hat{\boldsymbol{\psi}}_\mathrm{R}^\mathrm{T}\mathbf{J}\hat{\boldsymbol{\psi}}_\mathrm{R} = 0$. Based on this fact, the observer gain matrix is selected as

$$\boldsymbol{K} = \frac{\boldsymbol{G}\hat{\boldsymbol{\psi}}_\mathrm{R}\hat{\boldsymbol{\psi}}_\mathrm{R}^\mathrm{T}}{\|\hat{\boldsymbol{\psi}}_\mathrm{R}\|^2} \tag{15}$$

where $\boldsymbol{G} = g_1\mathbf{I} + g_2\mathbf{J}$ is a gain matrix and $\hat{\boldsymbol{\psi}}_\mathrm{R}\hat{\boldsymbol{\psi}}_\mathrm{R}^\mathrm{T}/\|\hat{\boldsymbol{\psi}}_\mathrm{R}\|^2$ is the orthogonal projection matrix, which takes the vector projection of the estimation error in the direction of $\hat{\boldsymbol{\psi}}_\mathrm{R}$.

The observer gain matrix $\boldsymbol{K}$ does not have a complex equivalent, because it cannot be expressed as a linear combination of matrices $\mathbf{I}$ and $\mathbf{J}$. This is why real space vectors were chosen rather than complex space vectors. If the observer is implemented in estimated rotor-flux coordinates, i.e., $\omega_\mathrm{k} = \hat{\omega}_\mathrm{s} = \mathrm{d}\hat{\vartheta}_\mathrm{s}/\mathrm{d}t$, then (15) simplifies to

$$\boldsymbol{K} = \begin{bmatrix} g_1 & 0 \\ g_2 & 0 \end{bmatrix} \tag{16}$$

since $\hat{\boldsymbol{\psi}}_\mathrm{R} = [\|\hat{\boldsymbol{\psi}}_\mathrm{R}\|, 0]^\mathrm{T}$. The gain matrix $\boldsymbol{G}$ is invariant of the coordinate system selected.

A gain selection in the form (15) makes the observer independent of the rotor speed estimate, but the gain matrix $\boldsymbol{G}$ determines the stability (and other properties) of the observer. As shown in Appendix A, the closed-loop system consisting of (4), (9), and (15) is locally stable in every operating point if (and only if) this gain matrix is given by

$$\boldsymbol{G} = \left[b\mathbf{I} + \left(\frac{c}{\hat{\omega}_\mathrm{s}} - \hat{\omega}_\mathrm{s}\right)\mathbf{J}\right]\frac{\alpha\mathbf{I} + \hat{\omega}_\mathrm{m}\mathbf{J}}{\alpha^2 + \hat{\omega}_\mathrm{m}^2} \tag{17}$$

where the coefficients $b > 0$ and $c > 0$ may depend on the operating point.[2] The observer gain design problem is reduced to the selection of the two positive coefficients b and c, which are actually the coefficients of the characteristic polynomial of the linearized closed-loop system, cf. Appendix A. An accurate stator-resistance estimate $\hat{R}_\mathrm{s}$ was assumed in the derivation of (17), but this assumption will be lifted, as will be described in Section V. The stability conditions corresponding to the gain (17) were originally presented in [7].

IV. Observer Design

A. Conventional Observer Gain Selections

The stage is set for observer gain selection by reviewing a few previously proposed gain selections. In [1], the angular speed of the rotor flux was estimated by means of the voltage model, while the magnitude estimation of the rotor flux was based on the current model. This design corresponds to the gain selection

$$\boldsymbol{G} = \mathbf{I}. \tag{18}$$

The corresponding coefficients in (17) are $b = \alpha$ and $c = \hat{\omega}_\mathrm{s}\hat{\omega}_\mathrm{r}$, where the angular slip frequency estimate is $\hat{\omega}_\mathrm{r} = \hat{\omega}_\mathrm{s} - \hat{\omega}_\mathrm{m}$. Coefficient c becomes negative at low speeds in the regenerating mode, indicating an unstable region as also reported in [1]. Therefore, gain selection (18) is not recommended.

In [4], it was shown that the stability problem appearing with the gain (18) can be remedied using

$$\boldsymbol{G} = k\left[\mathbf{I} + (\hat{\omega}_\mathrm{m}/\alpha)\mathbf{J}\right] \tag{19}$$

where k is a positive constant. This gain selection corresponds to the coefficients $b = (k/\alpha)(\alpha^2 + \hat{\omega}_\mathrm{m}^2)$ and $c = \hat{\omega}_\mathrm{s}^2$, which are always positive, except for $\hat{\omega}_\mathrm{s} = 0$ yielding $c = 0$. Stability is guaranteed in theory but, unfortunately, sufficient damping cannot be achieved using this design: selecting a small k results in an approximate voltage model, while a larger k results in too high a gain and noise amplification. A gain similar to (19) was in [17] found to stabilize a so-called statically compensated voltage model.

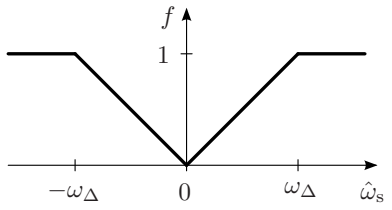

Fig. 3. Function f.

B. Proposed Observer Gain Selection

Even if the gain selection (19) results in a stable system, the effect of parameter errors on the accuracy at low speeds and the damping at higher speeds can be improved. Furthermore, the norm of the observer gain should not be too high, so as to avoid noise amplification. In order to integrate a simple and understandable design with these goals, the classical approach of mimicking the current model at low speeds and the voltage model at high speeds is adopted. This is made in conjunction with the previously derived stabilizing gain selection (17) by selecting the coefficients as

$$b = (1 - f)\alpha + f|\hat{\omega}_\mathrm{m}| \tag{20a}$$

$$c = \hat{\omega}_\mathrm{s}\left\{(1 - f)|\hat{\omega}_\mathrm{r}|\,\mathrm{sign}(\hat{\omega}_\mathrm{s}) + f[\hat{\omega}_\mathrm{s} + \alpha\,\mathrm{sign}(\hat{\omega}_\mathrm{s})]\right\}. \tag{20b}$$

The function f, shown in Fig. 3, is given by

$$f = \begin{cases} |\hat{\omega}_\mathrm{s}|/\omega_\Delta, & \text{if } |\hat{\omega}_\mathrm{s}| < \omega_\Delta \\ 1, & \text{if } |\hat{\omega}_\mathrm{s}| \geq \omega_\Delta \end{cases} \tag{21}$$

where ω_Δ is a positive constant, with a typical value of 0.1…0.5 p.u. Coefficients b and c in (20) are positive in every operating point, except that $c = 0$ for $\hat{\omega}_\mathrm{s} = 0$ by necessity, as mentioned previously.

[2] For $\hat{\omega}_\mathrm{s} = 0$, $c = 0$ has to be selected to avoid division by zero, giving only marginal stability for zero stator frequency.

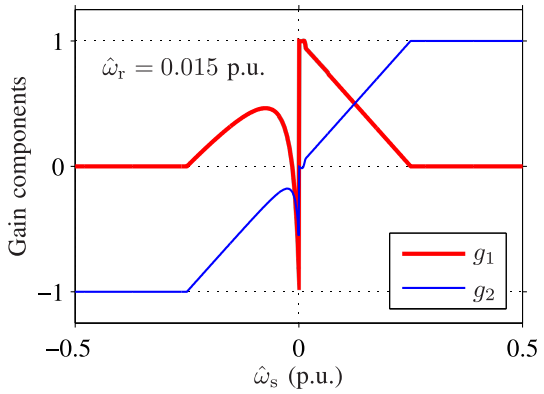

Fig. 4. Components of gain $\boldsymbol{G}$ evaluated using (17) and (20) with $\omega_\Delta = 0.25$ p.u. Parameters of a 45-kW IM were used. The angular slip frequency $\hat{\omega}_\mathrm{r} = 0.015$ p.u. equals the rated slip.

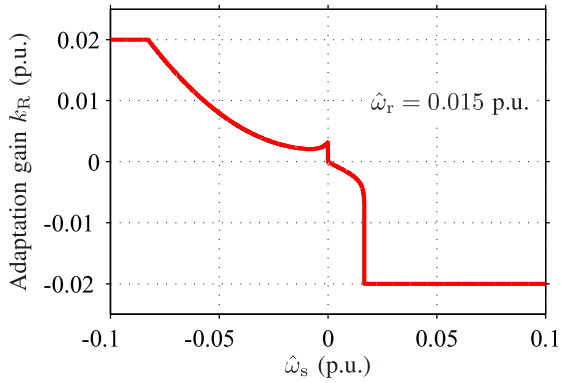

Fig. 5. Stator-resistance adaptation gain for a 45-kW IM when $k'_\mathrm{R} = 0.02$ p.u., $r = 0.2$, and $\omega_\Delta = 0.25$ p.u. The angular slip frequency $\hat{\omega}_\mathrm{r} = 0.015$ p.u. equals the rated slip.

At speeds above ω_Δ, the selection in (20) leads to $\boldsymbol{G} = \mathrm{sign}(\hat{\omega}_\mathrm{s})\mathbf{J}$, which yields sufficient damping while the effects of the parameter errors are similar to those of the pure voltage model. At the lowest speeds, $\boldsymbol{G} \approx \mathbf{I}$ in the motoring mode. As an example, the resulting gain components g_1 and g_2 are shown in Fig. 4 as a function of the stator frequency. The angular slip frequency estimate $\hat{\omega}_\mathrm{r} = \hat{\omega}_\mathrm{s} - \hat{\omega}_\mathrm{m}$ equals its rated value. It can be seen that, at low frequencies, the gains differ significantly in the regenerating mode (where $\omega_\mathrm{r}\omega_\mathrm{s} < 0$) and in the motoring mode.

V. Stator-Resistance Adaptation

The following stator-resistance adaptation law is proposed:

$$\frac{\mathrm{d}\hat{R}_\mathrm{s}}{\mathrm{d}t} = \boldsymbol{k}_\mathrm{R}^\mathrm{T}(\hat{\boldsymbol{e}} - \boldsymbol{e}') \tag{22a}$$

where $\boldsymbol{k}_\mathrm{R}$ is a gain vector. Similarly to the flux estimation, it is desirable that the stator-resistance adaptation is inherently sensorless. Hence, based on (8) and (14), the gain vector should be of the form

$$\boldsymbol{k}_\mathrm{R} = \frac{k_\mathrm{R}\hat{\boldsymbol{\psi}}_\mathrm{R}}{\|\hat{\boldsymbol{\psi}}_\mathrm{R}\|} \tag{22b}$$

where k_R is the adaptation gain.

As shown in Appendix B, the general stability conditions for the observer augmented with (22) are

$$k_\mathrm{R}\hat{\omega}_\mathrm{s}\hat{\omega}_\mathrm{r} < 0 \tag{23a}$$

$$k_\mathrm{R} < bL_\mathrm{M}/\|\hat{\boldsymbol{\psi}}_\mathrm{R}\| \tag{23b}$$

$$Ak_\mathrm{R}^2 + Bk_\mathrm{R} + C > 0 \tag{23c}$$

where the coefficients of the quadratic inequality in (23c) are

$$A = \left(\alpha^2 + \hat{\omega}_\mathrm{m}\hat{\omega}_\mathrm{r}\right)\left(\|\hat{\boldsymbol{\psi}}_\mathrm{R}\|/L_\mathrm{M}\right)^2$$
$$B = \left[\alpha(2\hat{\omega}_\mathrm{s}\hat{\omega}_\mathrm{r} - c) - b\left(\alpha^2 + \hat{\omega}_\mathrm{m}\hat{\omega}_\mathrm{r}\right)\right]\|\hat{\boldsymbol{\psi}}_\mathrm{R}\|/L_\mathrm{M}$$
$$C = \alpha bc.$$

where b and c are the positive design parameters in (17).

The stability conditions will be applied in the following. Based on the condition (23a), the sign of the gain k_R has to depend on the operating mode. Furthermore, the magnitude of k_R has to be limited according to (23c), while the condition (23b) is automatically fulfilled via (23a) and (23c).

It can be shown that the conditions in (23) are fulfilled by choosing

$$k_\mathrm{R} = \begin{cases} \min\{k'_\mathrm{R}, L_1\}, & \text{if } D > 0 \text{ and } \hat{\omega}_\mathrm{s}\hat{\omega}_\mathrm{r} \le 0 \\ \max\{-k'_\mathrm{R}, L_2\}, & \text{if } D > 0 \text{ and } \hat{\omega}_\mathrm{s}\hat{\omega}_\mathrm{r} > 0 \\ & \text{and } L_2 < 0 \\ -k'_\mathrm{R}\,\mathrm{sign}(\hat{\omega}_\mathrm{s}\hat{\omega}_\mathrm{r}), & \text{otherwise} \end{cases} \tag{24}$$

where k'_R is a positive design parameter and $D = B^2 - 4AC$. The limiting values are

$$L_1 = r\frac{-B - \sqrt{D}}{2A}, \quad L_2 = r\frac{-B + \sqrt{D}}{2A} \tag{25}$$

where the parameter $0 < r < 1$ affects the stability margin of the system; choosing $r = 1$ would lead to a marginally stable system (in the operating points where k_R is determined by L_1 or L_2). An example of the stator-resistance adaptation gain, corresponding to (20) and (24), is depicted in Fig. 5.

VI. Implementation

A. Estimated Rotor-Flux Coordinates

Observer (9) can be implemented in arbitrary coordinates. In the case of speed-sensorless drives and the gain matrix (15), the simplest equations are achieved in the estimated rotor-flux coordinates, where $\omega_\mathrm{k} = \hat{\omega}_\mathrm{s}$ and $\hat{\boldsymbol{\psi}}_\mathrm{R} = [\|\hat{\boldsymbol{\psi}}_\mathrm{R}\|, 0]^\mathrm{T}$. The estimated rotor-flux coordinates are favorable from the point of view of the discrete-time implementation as well.

The vector components in the estimated rotor-flux coordinates will be marked by the subscripts d and q, and the magnitude of the rotor-flux estimate will be denoted by $\hat{\psi}_\mathrm{R} = \|\hat{\boldsymbol{\psi}}_\mathrm{R}\|$. When the gain matrix (15) is used, the equations of the reduced-order observer (9) are

$$\frac{\mathrm{d}\hat{\psi}_\mathrm{R}}{\mathrm{d}t} = e'_\mathrm{d} + g_1(\hat{e}_\mathrm{d} - e'_\mathrm{d}) \tag{26a}$$

$$\frac{\mathrm{d}\hat{\vartheta}_\mathrm{s}}{\mathrm{d}t} = \frac{e'_\mathrm{q} + g_2(\hat{e}_\mathrm{d} - e'_\mathrm{d})}{\hat{\psi}_\mathrm{R}} = \hat{\omega}_\mathrm{s}. \tag{26b}$$

The components of the back EMF given in (7) become

$$e'_{\mathrm{d}} = u_{\mathrm{sd}} - \hat{R}_{\mathrm{s}} i_{\mathrm{sd}} - L_\sigma \frac{\mathrm{d}i_{\mathrm{sd}}}{\mathrm{d}t} + \hat{\omega}_{\mathrm{s}} L_\sigma i_{\mathrm{sq}} \tag{27a}$$

$$e'_{\mathrm{q}} = u_{\mathrm{sq}} - \hat{R}_{\mathrm{s}} i_{\mathrm{sq}} - L_\sigma \frac{\mathrm{d}i_{\mathrm{sq}}}{\mathrm{d}t} - \hat{\omega}_{\mathrm{s}} L_\sigma i_{\mathrm{sd}} \tag{27b}$$

and the d component of the back-EMF estimate in (8) is

$$\hat{e}_{\mathrm{d}} = R_{\mathrm{R}}(i_{\mathrm{sd}} - \hat{\psi}_{\mathrm{R}}/L_{\mathrm{M}}). \tag{28}$$

The components of the observer gain in (17) can be expressed as

$$g_1 = \frac{b\alpha - (c/\hat{\omega}_{\mathrm{s}} - \hat{\omega}_{\mathrm{s}})\hat{\omega}_{\mathrm{m}}}{\alpha^2 + \hat{\omega}_{\mathrm{m}}^2} \tag{29a}$$

$$g_2 = \frac{b\hat{\omega}_{\mathrm{m}} + (c/\hat{\omega}_{\mathrm{s}} - \hat{\omega}_{\mathrm{s}})\alpha}{\alpha^2 + \hat{\omega}_{\mathrm{m}}^2} \tag{29b}$$

The rotor-speed estimate is preferably computed by embedding (12) in a low-pass filter [16]

$$\frac{\mathrm{d}\hat{\omega}_{\mathrm{m}}}{\mathrm{d}t} = \alpha_{\mathrm{o}} \left(\hat{\omega}_{\mathrm{s}} - \frac{R_{\mathrm{R}} i_{\mathrm{sq}}}{\hat{\psi}_{\mathrm{R}}} - \hat{\omega}_{\mathrm{m}} \right) \tag{30}$$

where α_{o} is the filter bandwidth.

The stator-resistance adaptation law (22) in the estimated rotor-flux coordinates is

$$\frac{\mathrm{d}\hat{R}_{\mathrm{s}}}{\mathrm{d}t} = k_{\mathrm{R}} \left(\hat{e}_{\mathrm{d}} - e'_{\mathrm{d}} \right). \tag{31}$$

The adaptation should be disabled in the vicinity of no-load operation and at higher stator frequencies due to poor signal-to-noise ratio (which is a well-known fundamental property common to all speed-sensorless stator-resistance adaptation methods based only on the fundamental-wave excitation). Hence, parameter k'_{R} in (24) can be selected as

$$k'_{\mathrm{R}} = \begin{cases} k''_{\mathrm{R}}(1-f)|i_{\mathrm{sq}}|, & \text{if } |i_{\mathrm{sq}}| \geq i_\Delta \\ 0, & \text{if } |i_{\mathrm{sq}}| < i_\Delta \end{cases} \tag{32}$$

where k''_{R} is a positive constant. As seen from Fig. 3, the factor $1-f$ decreases linearly with the increasing absolute value of the stator frequency, being zero if $|\hat{\omega}_{\mathrm{s}}| \geq \omega_\Delta$.

B. Modeling of Magnetic Saturation

In speed-sensorless drives, the accuracy of the rotor-speed estimate depends on the rotor-resistance estimate, but the rotor-resistance estimate does not affect the field orientation in steady state [18], [19]. The stator-resistance adaptation (22) is also independent of the rotor-resistance estimate in steady state. Hence, the stator-resistance adaptation makes the field orientation almost immune to temperature variations.

However, the system is sensitive to the inductances L_σ and L_{M}, which vary due to the magnetic saturation (but do not depend on the temperature). If the magnetic saturation is not properly modeled, the field orientation becomes inaccurate and the stator-resistance estimate becomes dependent on the operating point.

With constant rotor-flux magnitude, the stator-flux magnitude

$$\psi_{\mathrm{s}} = \sqrt{(\psi_{\mathrm{R}} + L_\sigma i_{\mathrm{sd}})^2 + (L_\sigma i_{\mathrm{sq}})^2} \tag{33}$$

increases with increasing load (since $\psi_{\mathrm{R}} + L_\sigma i_{\mathrm{sd}}$ is constant while i_{sq} depends on the load). Since the state of saturation in the stator core mainly depends on the stator-flux magnitude [14], the magnetizing inductance L_{M} of the inverse-Γ model depends on the load (in addition to the main flux). Furthermore, if the machine is equipped with closed or skewed rotor slots, the dependency of the magnetizing inductance on the load is more pronounced [20].

In connection with reduced-order observers, the state variable $\hat{\psi}_{\mathrm{R}}$ and the measured stator-current magnitude i_{s} are convenient inputs of the saturation model. With this selection, algebraic loops and auxiliary variables can be avoided in the implementation. In the experiments, the saturation of L_σ and L_{M} was modeled as

$$\hat{L}_\sigma(\hat{\psi}_{\mathrm{R}}) = \frac{L_{\sigma\mathrm{u}}}{1 + \gamma L_{\sigma\mathrm{u}} \hat{\psi}_{\mathrm{R}}^2} \tag{34a}$$

$$\hat{L}_{\mathrm{M}}(\hat{\psi}_{\mathrm{R}}, i_{\mathrm{s}}) = \frac{L_{\mathrm{Mu}}}{1 + \beta \hat{\psi}_{\mathrm{R}}^S + \gamma L_{\mathrm{Mu}} (\hat{L}_\sigma i_{\mathrm{s}})^2} \tag{34b}$$

where $L_{\sigma\mathrm{u}}$ and L_{Mu} are the unsaturated values of the inductances and β, γ, and S are positive constants. If $\gamma = 0$ were chosen, the model of $\hat{L}_{\mathrm{M}}$ would correspond to that proposed in [21]. With positive γ, the magnetizing-inductance estimate decreases with increasing load.

C. Compensation for Inverter Nonlinearities

The stator voltage is not measured, but the reference voltage obtained from the current controller is used for the flux observer according to Fig. 2. The effect of inverter nonlinearities on the stator voltage is substantial at low speeds. Therefore, the most significant inverter nonlinearities, i.e. the dead-time effect and power device voltage drops, have to be compensated for [22], [23].

Using phase a as an example, a compensated duty cycle for the pulse-width modulator was evaluated as

$$d_{\mathrm{a}} = d_{\mathrm{a,ref}} + (2d_\delta/\pi) \arctan(i_{\mathrm{a}}/i_\delta) \tag{35}$$

where $d_{\mathrm{a,ref}}$ is the ideal duty cycle obtained from the current controller and i_{a} is the phase current. The parameter d_δ takes into account both the dead-time effect and the threshold voltage of the power devices, while the on-state slope resistance of the power devices is included in the stator-resistance estimate. The shape of the arctan function is determined by the parameter i_δ. The duty cycles of phases b and c were evaluated in a similar manner.

The current-feedforward compensation method in (35) corresponds to the method in [22], [23], except that the signum functions were replaced with the arctan functions in order to improve the performance in the vicinity of current zero crossings. It is worth noticing that the arctan function, multiplied by $2/\pi$, approaches the signum function as the parameter i_δ approaches zero.

VII. Experimental Setup and Parameters

The operation of the proposed observer and stator-resistance adaptation was investigated experimentally using the setup shown in Fig. 6. The speed-sensorless control system was

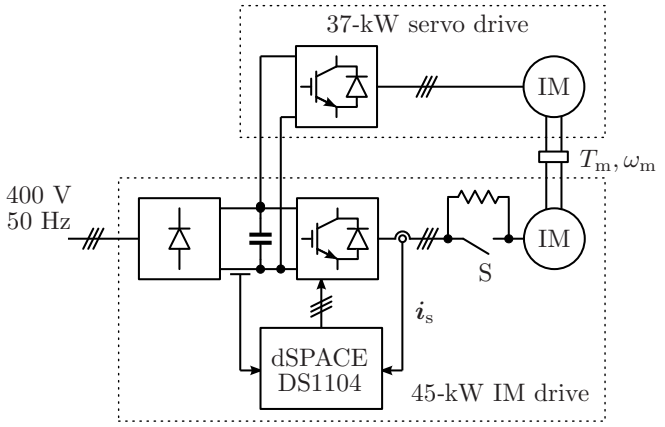

Fig. 6. Experimental setup. The stator currents and the DC-link voltage are used as feedback signals. Mechanical load is provided by a servo drive. The shaft torque T_m and the rotor speed ω_m are measured for monitoring purposes. Three-phase switch S is in the closed position, except in the experiment shown in Fig. 8.

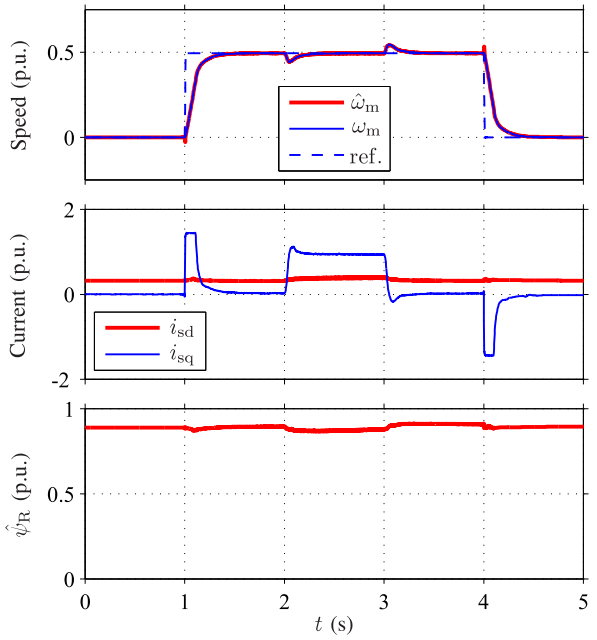

Fig. 7. Experimental results showing speed reference steps (0 → 750 rpm → 0). Rated load torque step is applied at $t = 2$ s and removed at $t = 3$ s.

implemented in a dSPACE DS1104 PPC/DSP board. A standard 45-kW four-pole IM (ABB M3GP225SMC4) is fed by a frequency converter that is controlled by the DS1104 board. The IM is equipped with closed and skewed rotor slots, and its rating is: speed 1477 r/min; frequency 50 Hz; line-to-line rms voltage 400 V; rms current 81 A; and torque 291 Nm. The base values for angular speed, voltage, and current are defined as $2\pi \cdot 50$ rad/s, $\sqrt{2/3} \cdot 400$ V, and $\sqrt{2} \cdot 81$ A, respectively.

A 37-kW servo-type IM is used as a loading machine. The shaft torque T_m and the rotor speed ω_m are measured using a HBM T10F torque flange and an incremental encoder, respectively, for monitoring purposes. The total moment of inertia of the experimental setup is 0.81 kgm^2 (1.66 times the inertia of the 45-kW IM rotor).

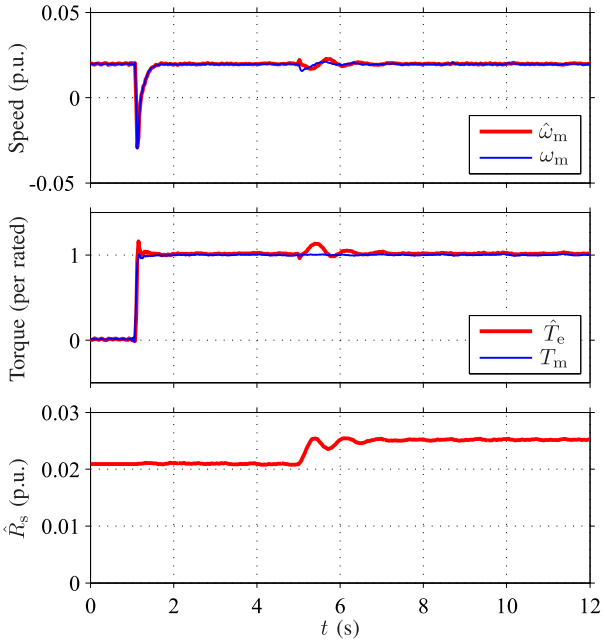

Fig. 8. Experimental results showing stepwise increase in the actual stator resistance at $t = 5$ s. Speed reference is kept at 30 rpm and a rated load torque is applied at $t = 1$ s.

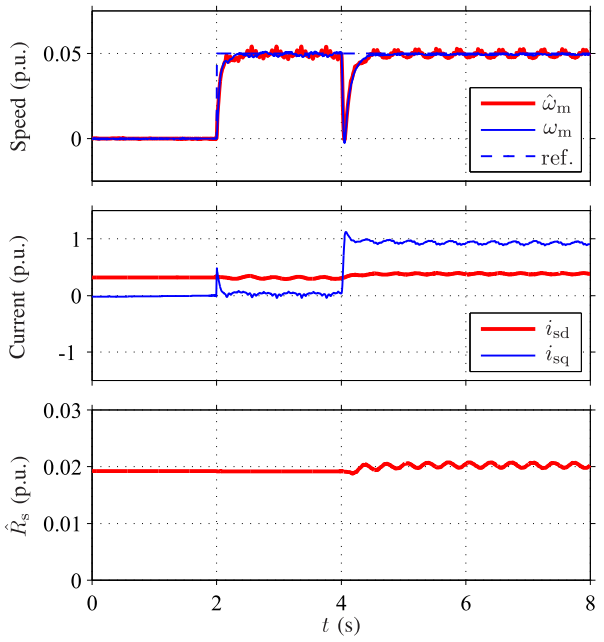

Fig. 9. Experimental results showing the effect of 0.02-p.u. DC offset in the a-phase current measurement channel.

The stator resistance of the 45-kW IM is approximately 55 mΩ at room temperature. Additional 10-mΩ 100-W resistors were added between the frequency converter and the IM. The resistance can be changed stepwise by opening or closing a manually operated three-phase switch (S) connected in parallel with the resistors. Unless otherwise noted, switch S is in the closed position.

The block diagram of the speed-sensorless control system implemented in the DS1104 board is shown in Fig. 2. The

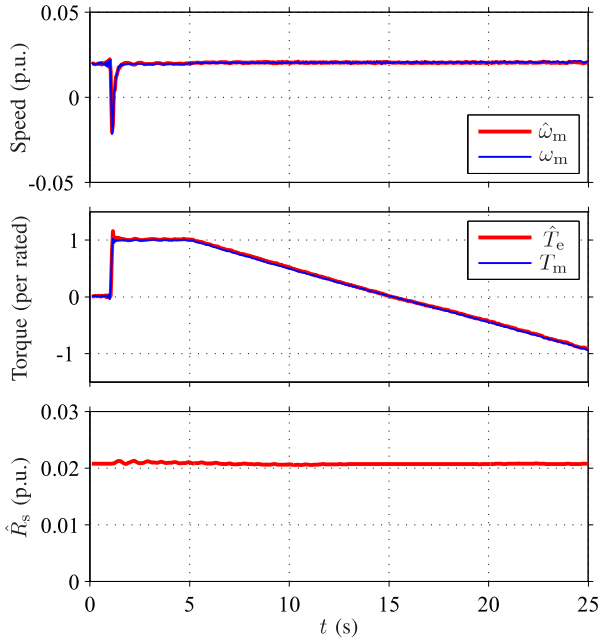

Fig. 10. Experimental results showing slow torque reversal when the speed reference is kept at 30 rpm.

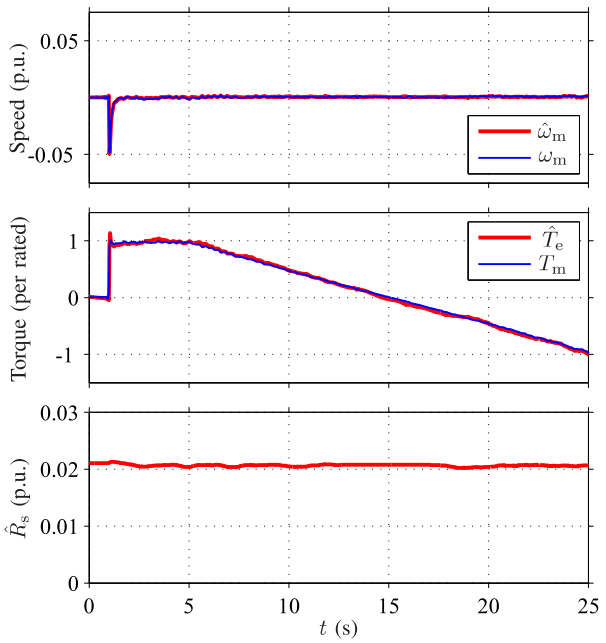

Fig. 11. Experimental results showing slow torque reversal when the speed reference is kept at 0 rpm.

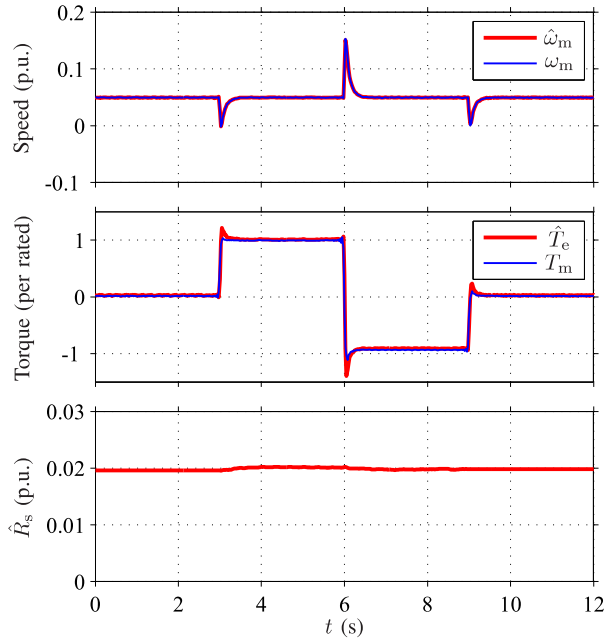

Fig. 12. Experimental results showing load-torque steps (0 → rated → negative rated → 0) when the speed reference is kept at 75 rpm.

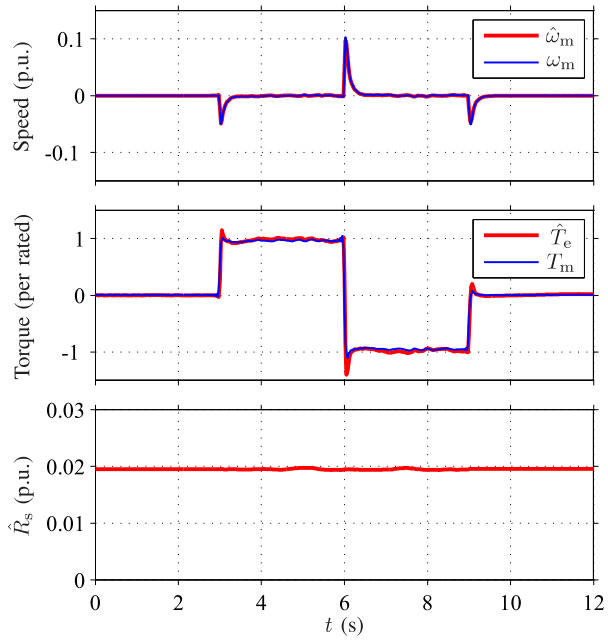

Fig. 13. Experimental results showing load-torque steps (0 → rated → negative rated → 0) when the speed reference is kept at 0 rpm.

stator currents and the DC-link voltage are measured, and the reference voltage obtained from the current controller is used for the flux observer. The sampling is synchronized to the modulation, and both the switching frequency and the sampling frequency are 4 kHz. The parameters for compensation of inverter nonlinearities in (35) are $d_\delta = 1.41\%$ and $i_\delta = 0.03$ p.u. A proportional-plus-integral (PI) synchronous-frame current controller is used. The control system shown in Fig. 2 is augmented with a speed controller, whose feedback signal is the speed estimate $\hat{\omega}_m$ obtained from the proposed observer. The bandwidth of this PI speed controller, including active damping [16], is 0.05 p.u.

The proposed observer was implemented in the estimated rotor-flux coordinates as described in Section VI. The per-unit parameters used in the experiments are: $R_R = 0.01$ p.u., $L_{Mu} = 3.02$ p.u., $L_{\sigma u} = 0.32$ p.u., $S = 8$, $\beta = 0.135$ p.u., and $\gamma = 1.5$ p.u. The coefficients in (20) are determined by the transition frequency $\omega_\Delta = 0.25$ p.u. The parameters needed for the stator-resistance adaptation are: $r = 0.2$ in (25) and $k''_R = 0.02$ p.u. and $i_\Delta = 0.2$ p.u. in (32). The bandwidth $\alpha_o = 6$

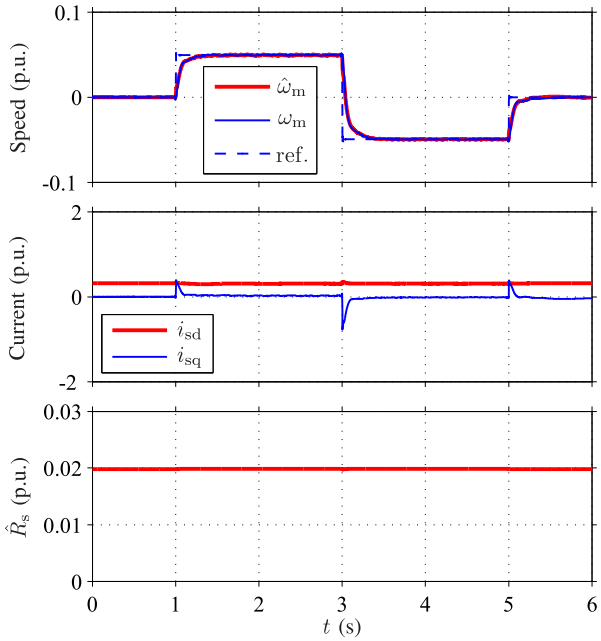

Fig. 14. Experimental results showing speed-reference steps (0 → 75 rpm → −75 rpm → 0) under no-load condition.

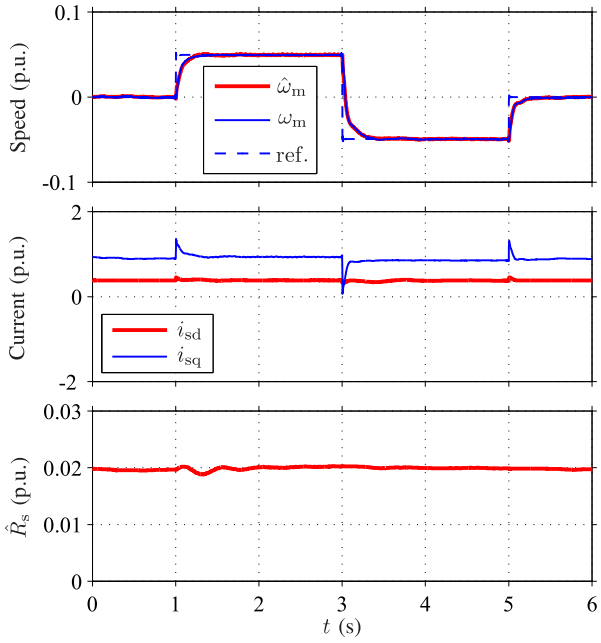

Fig. 15. Experimental results showing speed-reference steps (0 → 75 rpm → −75 rpm → 0) under rated load torque.

p.u. is used for the low-pass filter in (30). The estimate of the per-unit electromagnetic torque is evaluated as $\hat{T}_e = \hat{\psi}_R i_{sq}$.

VIII. Experimental Results

Fig. 7 shows results of medium-speed operation. The speed reference was stepped from 0 to 750 rpm and back to 0. A rated load torque step was applied at $t = 2$ s and removed at $t = 3$ s. According to (32), the stator-resistance adaptation was only active in the beginning of the acceleration and at the

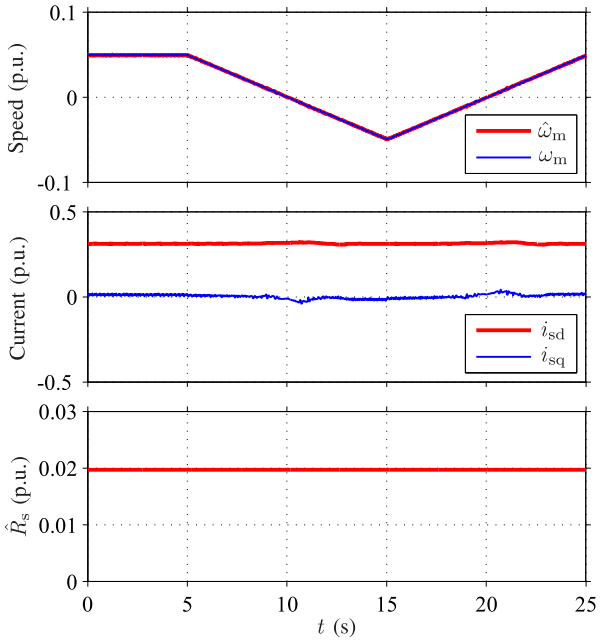

Fig. 16. Experimental results showing slow speed reversals (75 rpm → −75 rpm → 75 rpm) at no load.

end of the deceleration. It can be seen that the system is well damped.

Fig. 8 shows the stepwise change in the stator resistance (as seen by the frequency converter). Initially, three-phase switch S, cf. Fig. 6, was in the closed position. The speed reference was kept at 30 rpm. A rated-load torque step was applied at $t = 1$ s. Switch S was opened at $t = 5$ s, causing a 0.004-p.u. increase (corresponding to 20%) in the actual stator resistance. It can be seen that the stator-resistance estimate tracks the change in the actual stator resistance.

Fig. 9 shows the effect of a high DC offset in the current measurent. A DC offset of 0.02-p.u. (corresponding to 2.3 A) was intentionally added to the current-measurement channel of phase a. The speed reference was stepped from 0 to 75 rpm at $t = 2$ s. A rated load torque step was applied at $t = 4$ s. Due to the DC offset, some ripple having the frequency of 2.5 Hz (corresponding to 0.05 p.u.) can be seen in the speed and stator-resistance estimates. However, since the observer is well damped, the system is stable and no drifting problems appear despite the DC offset. It is to be noted that no offset compensators or estimators were used, but the implementation corresponds to that described in Sections VI and VII.

Results of a slow load-torque reversal are shown in Fig. 10. The speed reference was kept at 30 rpm. It can be seen that the torque estimate corresponds very well to the actual measured torque, indicating proper field orientation in the whole torque range. Fig. 11 shows results of a slow torque reversal when the speed reference was kept at 0 rpm. In the vicinity of zero stator frequency, the torque estimate differs slightly from the measured torque but the system remains stable.

Figs. 12 and 13 show load-torque steps when the speed reference was kept at 75 rpm and 0 rpm, respectively. The load torque was stepped to the rated value at $t = 3$ s, reversed

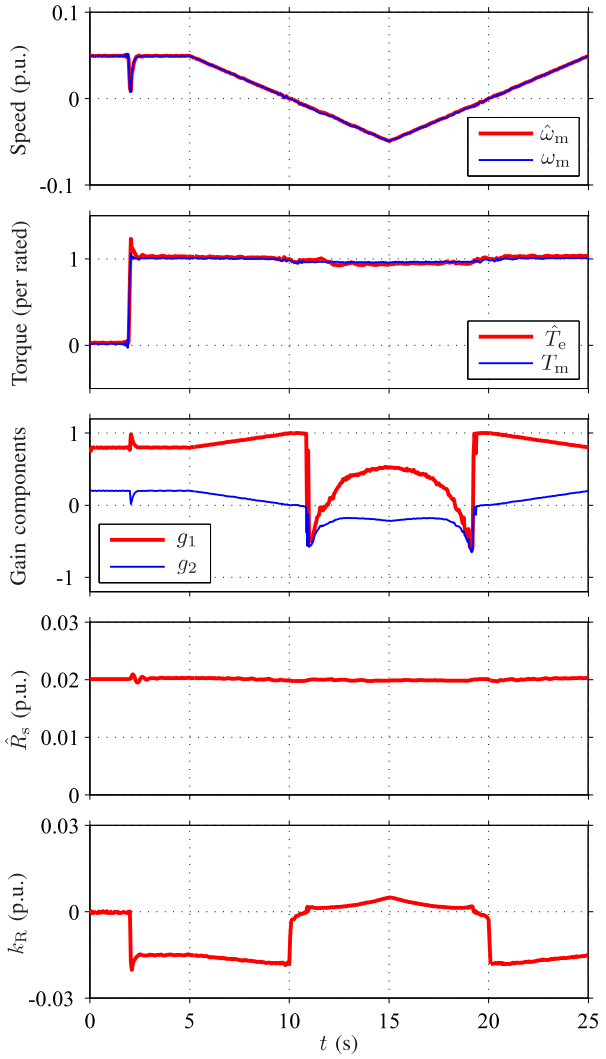

Fig. 17. Experimental results showing slow speed reversals (75 rpm $\rightarrow -75$ rpm $\rightarrow$ 75 rpm). The rated-load torque step is applied at $t = 2$ s.

at $t = 6$ s, and removed at $t = 9$ s. It can be seen that the proposed observer behaves well in torque transients even at zero speed.

Figs. 14 and 15 show speed-reference steps at low speeds in no-load condition and under the rated load torque, respectively. At $t = 1$ s, the speed reference was stepped from 0 to 75 rpm. The speed reference was reversed at $t = 3$ s and stepped to 0 at $t = 3$ s. It can be seen that the proposed observer behaves well in speed transients both in no-load and rated-load conditions.

Results of slow speed reversals at low speeds under no-load condition and under rated-load condition are shown in Figs. 16 and 17, respectively. The speed reference was slowly ramped from 75 rpm to -75 rpm and then back to 75 rpm. It can be seen that the system is stable under both loading conditions.

The sequence shown in Fig. 17 is a very challenging and revealing test for any speed-sensorless observer since all operating modes (motoring, plugging, and regenerating) are gone through. The gain components g_1 and g_2 and the adaptation gain k_R during the sequence are also depicted. Without the stabilizing observer gain (29), this kind of speed reversals would not be possible. Furthermore, without the stator-resistance adaptation, a very accurate stator-resistance estimate would be needed since the stator frequency remains in the vicinity of zero for a long time.

IX. Conclusions

In this paper, analytical stability conditions and design rules are derived for the reduced-order observer augmented with the stator-resistance adaptation. A general stabilizing gain for sensorless reduced-order observers is presented. A stator-resistance adaptation law is proposed, and stability conditions are derived for the system augmented with the resistance adaptation. Based on these stability conditions, an easy-to-tune observer design is proposed. The proposed design is comparatively simple, and it results in a robust and well-damped closed-loop system. Performance of the proposed observer design was evaluated using laboratory experiments with a 45-kW IM drive. Stable operation at very low speeds under different loading conditions was demonstrated. Furthermore, it was experimentally verified that the stator-resistance estimate can track stepwise changes in the actual resistance.

Appendix A
Derivation of a Stabilizing Observer Gain

From (4) and (9), the nonlinear dynamics of the estimation error are obtained:

$$\frac{\mathrm{d}\tilde{\boldsymbol{\psi}}_\mathrm{R}}{\mathrm{d}t} + \omega_\mathrm{k}\mathbf{J}\tilde{\boldsymbol{\psi}}_\mathrm{R} = -\boldsymbol{K}\left(\alpha\mathbf{I} - \omega_\mathrm{m}\mathbf{J}\right)\tilde{\boldsymbol{\psi}}_\mathrm{R} + \boldsymbol{K}\mathbf{J}\hat{\boldsymbol{\psi}}_\mathrm{R}\tilde{\omega}_\mathrm{m} + \left(\boldsymbol{K} - \mathbf{I}\right)\boldsymbol{i}_\mathrm{s}\tilde{R}_\mathrm{s} \tag{36}$$

where $\tilde{\boldsymbol{\psi}}_\mathrm{R} = \hat{\boldsymbol{\psi}}_\mathrm{R} - \boldsymbol{\psi}_\mathrm{R}$ is the estimation error of the rotor flux and $\tilde{R}_\mathrm{s} = \hat{R}_\mathrm{s} - R_\mathrm{s}$ is the error in the stator resistance estimate. The local stability of the system (36) can be studied via small-signal linearization in the synchronous coordinates. When $\tilde{R}_\mathrm{s} = 0$ is assumed and the observer gain (15) is applied in (36), linearization results in

$$\frac{\mathrm{d}\tilde{\boldsymbol{\psi}}_\mathrm{R}}{\mathrm{d}t} = \begin{bmatrix} -g_{10}\alpha & -g_{10}\omega_\mathrm{m0} + \omega_\mathrm{s0} \\ -g_{20}\alpha - \omega_\mathrm{s0} & -g_{20}\omega_\mathrm{m0} \end{bmatrix}\tilde{\boldsymbol{\psi}}_\mathrm{R} = \boldsymbol{A}\tilde{\boldsymbol{\psi}}_\mathrm{R} \tag{37}$$

where the operating-point quantities are marked by the subscript 0.

Since accurate parameter estimates are assumed, $\tilde{\boldsymbol{\psi}}_\mathrm{R0} = 0$ and $\hat{\omega}_\mathrm{m0} = \omega_\mathrm{m0}$ hold in the operating point. Therefore, the linearization is valid even if the gain $\boldsymbol{G}$ is a function of the rotor speed estimate $\hat{\omega}_\mathrm{m}$ and the angular frequency $\hat{\omega}_\mathrm{s}$ of the rotor flux estimate. The characteristic polynomial is $\det(s\mathbf{I} - \boldsymbol{A}) = s^2 + b_0 s + c_0$, where

$$b_0 = g_{10}\alpha + g_{20}\omega_\mathrm{m0} \tag{38a}$$

$$c_0 = \omega_\mathrm{s0}(g_{20}\alpha - g_{10}\omega_\mathrm{m0} + \omega_\mathrm{s0}). \tag{38b}$$

The nonlinear closed-loop system (36) is locally stable if the coefficients of the characteristic polynomial are positive: $b_0 > 0$ and $c_0 > 0$. From (38), the general stabilizing gain can be solved:

$$\boldsymbol{G}_0 = \left[b_0\mathbf{I} + \left(\frac{c_0}{\omega_\mathrm{s0}} - \omega_\mathrm{s0}\right)\mathbf{J}\right]\frac{\alpha\mathbf{I} + \omega_\mathrm{m0}\mathbf{J}}{\alpha^2 + \omega_\mathrm{m0}^2}. \tag{39}$$

The closed-loop poles of the system are

$$s_{1,2} = \frac{-b_0 \pm \sqrt{b_0^2 - 4c_0}}{2}. \tag{40}$$

APPENDIX B
STABILITY OF STATOR-RESISTANCE ADAPTATION

Assuming constant R_s and the stator-resistance adaptation law (22), the nonlinear dynamics of the stator resistance estimation error become

$$\frac{\mathrm{d}\tilde{R}_\mathrm{s}}{\mathrm{d}t} = \boldsymbol{k}_\mathrm{R}^\mathrm{T}\left(\hat{\boldsymbol{e}} - \boldsymbol{e}'\right) \tag{41}$$

The closed-loop system consisting of (36) and (41) can be linearized:

$$\frac{\mathrm{d}}{\mathrm{d}t}\begin{bmatrix}\tilde{\boldsymbol{\psi}}_\mathrm{R}\\ \tilde{R}_\mathrm{s}\end{bmatrix} = \underbrace{\begin{bmatrix}\boldsymbol{A} & (\boldsymbol{K}_0 - \mathbf{I})\,\boldsymbol{i}_\mathrm{s0}\\ -\boldsymbol{k}_\mathrm{R0}^\mathrm{T}(\alpha\mathbf{I} - \omega_\mathrm{m0}\mathbf{J}) & \boldsymbol{k}_\mathrm{R0}^\mathrm{T}\boldsymbol{i}_\mathrm{s0}\end{bmatrix}}_{\boldsymbol{A}'}\begin{bmatrix}\tilde{\boldsymbol{\psi}}_\mathrm{R}\\ \tilde{R}_\mathrm{s}\end{bmatrix}. \tag{42}$$

When the observer gain (15) is applied, the system matrix is

$$\boldsymbol{A}' = \begin{bmatrix}-g_{10}\alpha & -g_{10}\omega_\mathrm{m0} + \omega_\mathrm{s0} & (g_{10}-1)i_\mathrm{sd0}\\ -g_{20}\alpha - \omega_\mathrm{s0} & -g_{20}\omega_\mathrm{m0} & g_{20}i_\mathrm{sd0} - i_\mathrm{sq0}\\ -k_\mathrm{R0}\alpha & -k_\mathrm{R0}\omega_\mathrm{m0} & k_\mathrm{R0}i_\mathrm{sd0}\end{bmatrix} \tag{43}$$

where $i_\mathrm{sd0} = \|\boldsymbol{\psi}_\mathrm{R0}\|/L_\mathrm{M}$ and $i_\mathrm{sq0} = \omega_\mathrm{r0}\|\boldsymbol{\psi}_\mathrm{R0}\|/R_\mathrm{R}$. Using the Routh–Hurwitz stability criterion, the stability conditions are

$$k_\mathrm{R0}\omega_\mathrm{s0}\omega_\mathrm{r0} < 0 \tag{44a}$$

$$k_\mathrm{R0} < b_0/i_\mathrm{sd0} \tag{44b}$$

$$A_0 k_\mathrm{R0}^2 + B_0 k_\mathrm{R0} + C_0 > 0 \tag{44c}$$

where b_0 and c_0 are given in (38). The coefficients of the quadratic inequality in (44c) are

$$\begin{aligned} A_0 &= \left(\alpha^2 + \omega_\mathrm{m0}\omega_\mathrm{r0}\right) i_\mathrm{sd0}^2\\ B_0 &= \left[\alpha(2\omega_\mathrm{s0}\omega_\mathrm{r0} - c_0) - b_0\left(\alpha^2 + \omega_\mathrm{m0}\omega_\mathrm{r0}\right)\right] i_\mathrm{sd0}\\ C_0 &= \alpha b_0 c_0. \end{aligned}$$

ACKNOWLEDGMENT

The authors gratefully acknowledge the Academy of Finland for the financial support and ABB Oy for the experimental setup.

REFERENCES

[1] V. Ambrožič, D. Nedeljković, and J. Nastran, "Sensorless control of induction machine with parameter adaptation," in *Proc. IEEE ISIE'99*, vol. 2, Bled, Slovenia, July 1999, pp. 724–728.

[2] L. Harnefors, "Instability phenomena and remedies in sensorless indirect field oriented control," *IEEE Trans. Power Electron.*, vol. 15, no. 4, pp. 733–743, July 2000.

[3] S. Suwankawin and S. Sangwongwanich, "A speed-sensorless IM drive with decoupling control and stability analysis of speed estimation," *IEEE Trans. Ind. Electron.*, vol. 49, no. 2, pp. 444–455, Apr. 2002.

[4] S. Sangwongwanich, U. Nittayatareekul, and P. Magyar, "Direct speed estimation based on back EMF of induction motors – its equivalent MRAS representation and stability analysis," in *Proc. EPE'03*, Toulouse, France, Sept. 2003, CD-ROM.

[5] L. Harnefors, "Globally stable speed-adaptive observers for sensorless induction motor drives," *IEEE Trans. Ind. Electron.*, vol. 54, no. 2, pp. 1243–1245, Apr. 2007.

[6] S. Sangwongwanich, S. Suwankawin, S. Po-ngam, and S. Koonlaboon, "A unified speed estimation design framework for sensorless ac motor drives based on positive-real property," in *Proc. PCC-Nagoya'07*, Nagoya, Japan, Apr. 2007, pp. 1111–1118.

[7] L. Harnefors and M. Hinkkanen, "Complete stability of reduced-order and full-order observers for sensorless IM drives," *IEEE Trans. Ind. Electron.*, vol. 55, no. 3, pp. 1319–1329, Mar. 2008.

[8] J. Holtz and J. Quan, "Drift- and parameter-compensated flux estimator for persistent zero-stator-frequency operation of sensorless-controlled induction motors," *IEEE Trans. Ind. Appl.*, vol. 39, no. 4, pp. 1052–1060, July/Aug. 2003.

[9] P. L. Jansen and R. D. Lorenz, "A physically insightful approach to the design and accuracy assessment of flux observers for field oriented induction machine drives," *IEEE Trans. Ind. Appl.*, vol. 30, no. 1, pp. 101–110, Jan./Feb. 1994.

[10] M. Tsuji, S. Chen, K. Izumi, and E. Yamada, "A sensorless vector control system for induction motors using *q*-axis flux with stator resistance identification," *IEEE Trans. Ind. Electron.*, vol. 48, no. 1, pp. 185–194, Feb. 2001.

[11] M. Rashed and A. F. Stronach, "A stable back-EMF MRAS-based sensorless low-speed induction motor drive insensitive to stator resistance variation," *IEE Proc. Electr. Power Appl.*, vol. 151, no. 6, pp. 685–693, Nov. 2004.

[12] C. Lascu, I. Boldea, and F. Blaabjerg, "Very-low-speed variable-structure control of sensorless induction machine drives without signal injection," *IEEE Trans. Ind. Appl.*, vol. 41, no. 2, pp. 591–598, Mar./Apr. 2005.

[13] M. Saejia and S. Sangwongwanich, "Averaging analysis approach for stability analysis of speed-sensorless induction motor drives with stator resistance estimation," *IEEE Trans. Ind. Electron.*, vol. 53, no. 1, pp. 162–177, Feb. 2006.

[14] G. R. Slemon, "Modelling of induction machines for electric drives," *IEEE Trans. Ind. Appl.*, vol. 25, no. 6, pp. 1126–1131, Nov./Dec. 1989.

[15] G. C. Verghese and S. R. Sanders, "Observers for flux estimation in induction machines," *IEEE Trans. Ind. Electron.*, vol. 35, no. 1, pp. 85–94, Feb. 1988.

[16] L. Harnefors, "Design and analysis of general rotor-flux-oriented vector control systems," *IEEE Trans. Ind. Electron.*, vol. 48, no. 2, pp. 383–390, Apr. 2001.

[17] L. Harnefors and R. Ottersten, "Regeneration-mode stabilization of the 'statically compensated voltage model'," *IEEE Trans. Ind. Electron.*, vol. 54, no. 2, pp. 818–824, Apr. 2007.

[18] S. Sangwongwanich and S. Okuma, "A unified approach to speed and parameter identification of induction motor," in *Proc. IEEE IECON'91*, vol. 1, Kobe, Japan, Nov. 1991, pp. 712–715.

[19] H. Kubota and K. Matsuse, "Speed sensorless field-oriented control of induction motor with rotor resistance adaptation," *IEEE Trans. Ind. Appl.*, vol. 30, no. 5, pp. 1219–1224, Sept./Oct. 1994.

[20] T. Tuovinen, M. Hinkkanen, and J. Luomi, "Modeling of mutual saturation in induction machines," in *Conf. Rec. IEEE-IAS Annu. Meeting*, Edmonton, Canada, Oct. 2008, CD-ROM.

[21] H. C. J. de Jong, "Saturation in electrical machines," in *Proc. ICEM'80*, vol. 3, Athens, Greece, Sept. 1980, pp. 1545–1552.

[22] J. K. Pedersen, F. Blaabjerg, J. W. Jensen, and P. Thogersen, "An ideal PWM-VSI inverter with feedforward and feedback compensation," in *Proc. EPE'93*, vol. 4, Brighton, U.K., Sept. 1993, pp. 312–318.

[23] J.-W. Choi and S.-K. Sul, "Inverter output voltage synthesis using novel dead time compensation," *IEEE Trans. Power Electron.*, vol. 11, no. 2, pp. 221–227, Mar. 1996.

Marko Hinkkanen (M'06) received the M.Sc.(Eng.) and D.Sc.(Tech.) degrees from Helsinki University of Technology, Espoo, Finland, in 2000 and 2004, respectively. Since 2000, he has been with Helsinki University of Technology. He is currently an Adjunct Professor with the Department of Electrical Engineering, Helsinki University of Technology. His research interests are in the areas of electric drives and electric machines.

Lennart Harnefors (S'93–M'97–SM'07) was born in Eskilstuna, Sweden, in 1968. He received the M.Sc., Licentiate, and Ph.D. degrees in electrical engineering from the Royal Institute of Technology, Stockholm, Sweden, in 1993, 1995, and 1997, respectively, and the Docent (D.Sc.) degree in industrial automation from Lund University, Lund, Sweden, in 2000.

From 1994 to 2005, he was with Mälardalen University, Västerås, Sweden, where he, in 2001, was appointed as a Professor of electrical engineering. From 2001 to 2006, he was also a part-time Visiting Professor of electrical drives with Chalmers University of Technology, Göteborg, Sweden. He is currently with ABB Power Systems/HVDC, Ludvika, Sweden. His research interests include applied signal processing and control, in particular, control of power electronic systems and ac drives.

Dr. Harnefors is an Associate Editor of the IEEE TRANSACTIONS ON INDUSTRIAL ELECTRONICS and the *International Journal of Power Electronics*. He was the recipient of the 2000 ABB Gunnar Engström Energy Award and the 2002 IEEE TRANSACTIONS ON INDUSTRIAL ELECTRONICS Best Paper Award.

Jorma Luomi (M'92) is a Professor in the Department of Electrical Engineering, Helsinki University of Technology, Espoo, Finland. He joined Helsinki University of Technology in 1980, and from 1991 to 1998 he was a Professor at Chalmers University of Technology. His research interests are in the areas of electric drives, electric machines, and numerical analysis of electromagnetic fields. He received the M.Sc.(Eng.) and D.Sc.(Tech.) degrees from Helsinki University of Technology, in 1977 and 1984, respectively.